INTERNATIONAL JOURNAL FOR NUMERICAL METHODS IN FLUIDS
Int. J. Numer. Meth. Fluids 2009; **60**:177–202
Published online 6 August 2008 in Wiley InterScience (www.interscience.wiley.com). DOI: 10.1002/fld.1880

Experimental validation of two depth-averaged turbulence models

J. Fe[1,3,*,†], F. Navarrina[1,3], J. Puertas[2,3], P. Vellando[2,3] and D. Ruiz[1,3]

[1]*Grupo de Métodos Numéricos en Ingeniería, Spain*
[2]*Grupo de Ingeniería del Agua y del Medio Ambiente, Spain*
[3]*E.T.S. de Ingenieros de Caminos, Canales y Puertos, Universidad de A Coruña, Campus de Elviña, 15071 A Coruña, Spain*

SUMMARY

A finite volume turbulence model for the resolution of the two-dimensional shallow water equations with turbulent term is presented. After making a finite volume discretization of the depth-averaged k–ε equations in conservative form, the q–r equations, that give stability to the process, are obtained. Wall and inlet boundary conditions for the turbulent equations and wall conditions for the hydrodynamic equations are discussed. A comparison between the k–ε and q–r models and some experimental results is made. Copyright © 2008 John Wiley & Sons, Ltd.

Received 19 November 2007; Revised 4 June 2008; Accepted 5 June 2008

KEY WORDS: finite volume; shallow water; turbulence model; depth-averaged k–ε; q–r; friction velocity; wall conditions

1. INTRODUCTION

The two-dimensional shallow water equations (2D-SWE) are obtained from the three-dimensional Navier–Stokes equations by means of an average in time, an integration in depth and some simplifying hypothesis [1], the most important of which is the hydrostatic pressure distribution, that can be assumed when the vertical length scale is much smaller than the horizontal one. This set of equations describes remarkably well the fluid behavior when the ratio of the depth to the horizontal dimensions is small and the magnitude of the vertical velocity component is much smaller than the magnitude of the horizontal velocity components, at the space and time scales of

*Correspondence to: J. Fe, E.T.S. de Ingenieros de Caminos, Canales y Puertos, Universidad de A Coruña, Campus de Elviña, 15071 A Coruña, Spain.
†E-mail: jfe@udc.es

Contract/grant sponsor: Xunta de Galicia; contract/grant numbers: PGIDIT06TAM11801PR, PGIDIT05PXIC 118002PN
Contract/grant sponsor: Ministerio de Educación y Ciencia; contract/grant numbers: DPI2004-05156, DPI2006-15275, DPI2007-61214

interest for the resolution of a given problem. This situation can be found, for instance, in the flow in channels and rivers or tidal flows, which are the main fields of application for our work. Once the velocity field is known, many problems of great practical interest such as the sediment flow [2], the evolution of salt concentration in an estuary [3] or the pollutant diffusion [4] can also be solved.

Use of the 2D-SWE has not stopped to increase during the last few decades and finite volume discretizations have proved to be a useful tool, specially to apply these equations to unstructured grids. Most finite volume formulations for the 2D-SWE take advantage of the analogy between this system and the gas dynamics equations and have successfully been employed in the flow simulation. The finite volume method (FVM) is now probably the most widespread modelling strategy within the shallow water approximation [5] and it was the method used in our work.

2D-SWE take into account the effects of turbulence both through the frictional terms and the diffusion-like term, which involves second derivatives. Frictional terms quantify the turbulence effects in the vertical, while the second derivatives term quantifies the turbulent losses produced by the horizontal mixing of momentum. This last term may not be significant in many practical problems when we only need an estimation of energy losses. In problems in which recirculation zones do not appear, turbulent losses can be globally evaluated by an adequate choice of the friction coefficient. Also, in some tidal flows, the influence of turbulence in the mean-velocity field can be almost negligible [6]. For these reasons 2D-SWE are frequently used without considering the second derivatives (turbulent) term, either using first-order schemes [7, 8], second order [9, 10] or both first and second order [11, 12]. This simplification is reasonable in many cases but not always. Thus, in the simulation of flows in which recirculation zones play a significant role, the inclusion of this turbulent term may become very important.

When applying the FVM to the 2D-SWE, the numerical flux at the cell edges has to be calculated and the upwinding of the convective term has proved to be a useful technique [7, 8, 12]. Unfortunately, first-order upwind discretizations produce an amount of numerical viscosity (or diffusion) which in some cases may be of similar magnitude to the turbulent viscosity and can make it difficult to appreciate the effect of the turbulent term [13]. Among the authors using the 2D-SWE with turbulent term, Cea *et al.* [6] propose an hybrid algorithm (first order for the depth, second order for the velocity components) and Anastasiou *et al.* [14] use a second-order method. However, probably for the above reason, references of first-order methods, such as the one presented here, applied to these equations, have not been found.

The two-dimensional study of viscous fluids with Reynolds numbers below 10 000 can be very accurately solved by the utilization of constant values for the viscosity ν in the turbulent term [13], but in most cases of practical interest it is necessary to calculate the turbulent viscosity at every point, and a turbulence model is therefore needed. The well-known k–ε model has been used to obtain the turbulent viscosity by many researchers. The two-dimensional version of this model was obtained in the late 1970s by Rastogi and Rodi [15] from the Launder and Spalding three-dimensional model [16] and it was applied by [17, 18] with slight differences in the equations. More recently, it has been used by [4, 6, 19–21]. In these last cases the time derivatives of the turbulent variables are considered and discretized. It allows to know the time evolution of the variables and this approach has been followed. The implementation of the model is not straightforward, among other reasons because non-physical negative values can appear for the k and ε variables, causing instabilities and eventually stopping the process. As it will be shown, the q–r system is derived from the k–ε system with the aim of giving stability to the process and both approaches produce similar results. In this work the conservative form of the k–ε and q–r equations will be used.

DOI: 10.1002/fld

In this paper we compare the performance of these two models, we check the computed results with experimental measures and we discuss some boundary conditions. The work is distributed as follows. In Section 2 the hydrodynamic equations are presented and their discretization is summarized. In Section 3 the k–ε equations in conservative form are discretized. In Section 4 the q–r equations are obtained. Some boundary conditions for the hydrodynamic and turbulent equations are discussed in Section 5 as well as a method to calculate the friction velocity. In Section 6 a comparison is made between the results of the k–ε and the q–r models and some experimental measures.

2. THE HYDRODYNAMIC EQUATIONS

2.1. The shallow water equations with turbulent term

The 2D-SWE system in conservative form is expressed as

$$\frac{\partial \mathbf{U}}{\partial t}+\frac{\partial \mathbf{F_1}}{\partial x}+\frac{\partial \mathbf{F_2}}{\partial y}=\mathbf{G} \tag{1}$$

being the vector of unknowns $\mathbf{U}$ and the flux terms

$$\mathbf{U}=\begin{pmatrix} h \\ hu \\ hv \end{pmatrix}, \quad \mathbf{F_1}=\begin{pmatrix} hu \\ hu^2+\frac{1}{2}gh^2 \\ huv \end{pmatrix}, \quad \mathbf{F_2}=\begin{pmatrix} hv \\ huv \\ hv^2+\frac{1}{2}gh^2 \end{pmatrix} \tag{2}$$

and being the source term

$$\mathbf{G}=\begin{pmatrix} 0 \\ gh(S_{0x}-S_{fx})+S_{t1} \\ gh(S_{0y}-S_{fy})+S_{t2} \end{pmatrix} \tag{3}$$

in which both the Coriolis and the wind stresses terms have been neglected. The reason is that the Coriolis term has little significance when applied to small domains and the wind term influence is not relevant in some situations such as indoor laboratory channels. In the above expressions h is the fluid depth, u and v are the horizontal velocity components and g is the gravity acceleration. The geometric slopes S_{0x}, S_{0y} are expressed in terms of H (see Figure 1) as

$$S_{0x}=\frac{\partial H}{\partial x}, \quad S_{0y}=\frac{\partial H}{\partial y} \tag{4}$$

S_{fx}, S_{fy} are the friction slopes, whose values, according to the Manning's formula [12, 22], are

$$S_{fx}=\frac{n^2 u\sqrt{u^2+v^2}}{R_h^{4/3}}, \quad S_{fy}=\frac{n^2 v\sqrt{u^2+v^2}}{R_h^{4/3}} \tag{5}$$

DOI: 10.1002/fld

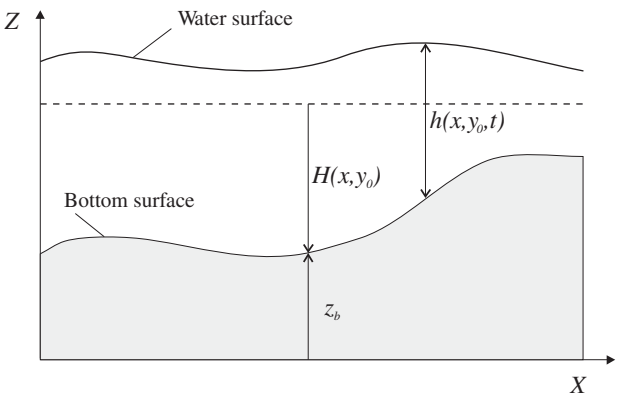

Figure 1. Representation of the variables H and h.

where R_h is the hydraulic radius. Finally, S_{t1}, S_{t2} are the turbulent terms

$$S_{t1} = \frac{\partial}{\partial x}\left(2\nu_t h \frac{\partial u}{\partial x}\right) + \frac{\partial}{\partial y}\left(\nu_t h\left[\frac{\partial v}{\partial x} + \frac{\partial u}{\partial y}\right]\right) \tag{6}$$

$$S_{t2} = \frac{\partial}{\partial x}\left(\nu_t h\left[\frac{\partial v}{\partial x} + \frac{\partial u}{\partial y}\right]\right) + \frac{\partial}{\partial y}\left(2\nu_t h \frac{\partial v}{\partial y}\right) \tag{7}$$

that quantify the energy dissipation due to the turbulent interactions among the particles. The eddy viscosity ν_t is another unknown of the problem.

2.2. The finite volume mesh

The finite volume mesh used in this work is based on a triangular discretization of the domain so that the nodes of the triangular mesh are used as the nodes of the finite volume mesh (see Figure 2).

For each node I, the barycenters of all the triangles that have the common vertex I as well as the mid-points of the corresponding edges are considered. The boundary Γ_i of the cell C_i is defined by these points. By $\Gamma_{ij} = \overline{\mathrm{AMB}}$ we represent the part of Γ_i that is also part of Γ_j. The outward normal vector to Γ_{ij} is $\boldsymbol{\eta}_{ij}$. The norm of $\boldsymbol{\eta}_{ij}$, $\|\boldsymbol{\eta}_{ij}\|$, is the length of the edge and $\widetilde{\boldsymbol{\eta}}_{ij}$ is the corresponding unit vector. The vector $\boldsymbol{\eta}_{ij}$ can have different magnitude and direction at each pair of segments $\overline{\mathrm{AM}}$ and $\overline{\mathrm{MB}}$, thus

$$\boldsymbol{\eta}_{ij} = \begin{cases} \boldsymbol{\eta}_{ij}^{\mathrm{AM}} & \text{at } \overline{\mathrm{AM}} \\ \boldsymbol{\eta}_{ij}^{\mathrm{MB}} & \text{at } \overline{\mathrm{MB}} \end{cases} \tag{8}$$

The subcell T_{ij} is the union of triangles AMI and MBI.

DOI: 10.1002/fld

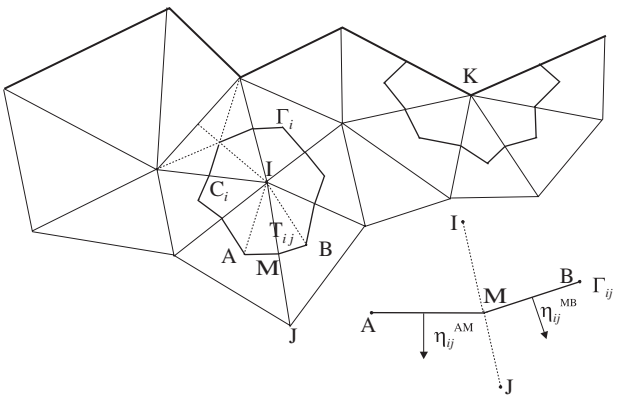

Figure 2. Finite volume construction.

2.3. Discretization of the hydrodynamic equations

At this point we wish to integrate the 2D-SWE, what results in

$$\iint_{C_i} \frac{\partial \mathbf{U}}{\partial t} \mathrm{d}A + \iint_{C_i} \nabla \cdot \mathscr{F} \, \mathrm{d}A = \iint_{C_i} \mathbf{G} \, \mathrm{d}A \tag{9}$$

where the operator ∇ stands for $(\partial/\partial x, \partial/\partial y)$ and $\mathscr{F} = (\mathbf{F_1}, \mathbf{F_2})$. If we apply the Gauss theorem to the flux term, it results

$$\iint_{C_i} \frac{\partial \mathbf{U}}{\partial t} \mathrm{d}A + \int_{\Gamma_i} \mathscr{F} \cdot \tilde{\boldsymbol{\eta}} \, \mathrm{d}l = \iint_{C_i} \mathbf{G} \, \mathrm{d}A \tag{10}$$

The details on the application of the FVM to the 2D-SWE, by making use of the upwind Van Leer Q-scheme [7, 23], can be found in [13]. The discretized expression of the 2D-SWE that corresponds to node I is

$$\frac{\mathbf{U}_i^{n+1} - \mathbf{U}_i^n}{\Delta t} A_i + \sum_{j \in \mathscr{K}_i} \|\boldsymbol{\eta}_{ij}\| \boldsymbol{\phi}_{ij}^n = \sum_{j \in \mathscr{K}_i} (A_{ij} \boldsymbol{\psi}_{ij}^n + \|\boldsymbol{\eta}_{ij}\| \boldsymbol{\psi}_{vij}^n) \tag{11}$$

in which $\mathbf{U}_i^n$ and $\mathbf{U}_i^{n+1}$ are approximations to the solution of equation (1) within each cell C_i and at time steps t_n and t_{n+1}. A_i and A_{ij} are the cell and subcell areas. $\mathscr{K}_i$ represents the set of neighboring nodes of I. The numerical flux $\boldsymbol{\phi}_{ij}^n$ is the approximation of $\mathbf{Z} = \mathscr{F} \cdot \tilde{\boldsymbol{\eta}}$, at Γ_{ij}, $j \in \mathscr{K}_i$ and at $t = t_n$, and it is given by

$$\boldsymbol{\phi}_{ij}^n = \frac{\mathbf{Z}(\mathbf{U}_i^n, \tilde{\boldsymbol{\eta}}_{ij}) + \mathbf{Z}(\mathbf{U}_j^n, \tilde{\boldsymbol{\eta}}_{ij})}{2} - c_d \frac{1}{2} |\mathbf{Q}(\mathbf{U}_Q^n, \tilde{\boldsymbol{\eta}}_{ij})| (\mathbf{U}_j^n - \mathbf{U}_i^n) \tag{12}$$

where c_d $(0 \leqslant c_d \leqslant 1)$ is a coefficient [13] whose meaning and utility are summarized next.

When working with a Roe-type scheme, like the one used here, the expression of the flux at a cell interface can be interpreted as the sum of a centered average of the fluxes on both sides of the boundary plus an upwinding term. This term stabilizes the system at the expense of introducing

DOI: 10.1002/fld

a certain amount of numerical viscosity (or diffusion). A way to make the model less diffusive is to reduce the upwinding term as much as possible by using a coefficient c_d. Its optimal value is the smallest that can provide stable calculations and decreases with the mesh size. If $c_d = 0$, the scheme is a centered one. If $c_d = 1$, there is no upwinding term reduction. In the Cavity Flow problem, which was used to test the effectiveness of employing this coefficient, the value $c_d = 0.03$ was chosen.

Q is the jacobian matrix of **Z**

$$\mathbf{Q} = \frac{\mathrm{d}\mathbf{Z}}{\mathrm{d}\mathbf{U}} = \widetilde{\alpha}\frac{\mathrm{d}\mathbf{F_1}}{\mathrm{d}\mathbf{U}} + \widetilde{\beta}\frac{\mathrm{d}\mathbf{F_2}}{\mathrm{d}\mathbf{U}} \tag{13}$$

being $\widetilde{\alpha}, \widetilde{\beta}$ the components of $\widetilde{\boldsymbol{\eta}}$ (the subscripts i, j are implied). $|\mathbf{Q}|$ is defined as

$$|\mathbf{Q}| = \mathbf{X}|\boldsymbol{\Lambda}|\mathbf{X}^{-1} \tag{14}$$

where $|\boldsymbol{\Lambda}|$ is the diagonal matrix given by the absolute values of the eigenvalues of **Q** and **X** is the eigenvectors matrix of **Q**. $\mathbf{U}_Q$ is defined by

$$\mathbf{U}_Q = \frac{\mathbf{U}_i + \mathbf{U}_j}{2} \tag{15}$$

The numerical source, at every subcell T_{ij} and at time step $t = t_n$, has two terms, as it can be seen in (11). In the first of them, the numerical source is calculated as

$$\boldsymbol{\psi}_{ij}^n = (\mathbf{I} - |\mathbf{Q}|\mathbf{Q}^{-1})\widehat{\mathbf{G}}_{\mathbf{0}} + \widehat{\mathbf{G}}_{\mathbf{f}} \tag{16}$$

where the numerical geometric slope $\widehat{\mathbf{G}}_{\mathbf{0}}$ and the numerical friction slope $\widehat{\mathbf{G}}_{\mathbf{f}}$ are

$$\widehat{\mathbf{G}}_{\mathbf{0}} = \begin{pmatrix} 0 \\ g\dfrac{h_i^n + h_j^n}{2}\dfrac{H_j - H_i}{d_{ij}}\widetilde{\alpha} \\ g\dfrac{h_i^n + h_j^n}{2}\dfrac{H_j - H_i}{d_{ij}}\widetilde{\beta} \end{pmatrix}, \quad \widehat{\mathbf{G}}_{\mathbf{f}} = \begin{pmatrix} 0 \\ gh_i^n(-S_{fx})_i^n \\ gh_i^n(-S_{fy})_i^n \end{pmatrix} \tag{17}$$

being d_{ij} the normal distance from I to Γ_{ij}, which has different values at $\overline{\mathrm{AMI}}$ and at $\overline{\mathrm{MBI}}$. It can be noted that the numerical geometric slope $\widehat{\mathbf{G}}_{\mathbf{0}}$ is upwinded [7], while the numerical friction slope $\widehat{\mathbf{G}}_{\mathbf{f}}$ is discretized pointwise [24], which is a widespread method to treat this term. It has recently been proposed [25] a unified discretization of the friction term, which consists in a similar numerical treatment of the flux, friction and other source terms in the equation. This unified approach improves the balance among the terms of the equation and has given better results than the pointwise discretization of the one-dimensional SWE, in cases of steady flow. However, in the proposed two-dimensional model, we have discretized pointwise for the sake of simplicity.

In the second term, the numerical source takes the form

$$\boldsymbol{\psi}_{vij}^n = \widehat{\mathbf{G}}_{\mathbf{t}} \tag{18}$$

DOI: 10.1002/fld

where the numerical turbulent slope is

$$\widehat{\mathbf{G}}_{\mathbf{t}}=\left\{\begin{array}{c} 0 \\ \dfrac{v_{ti}+v_{tj}}{2}\dfrac{h_i^n+h_j^n}{2}\left(2\dfrac{u_{xi}^n+u_{xj}^n}{2}\widetilde{\alpha}+\dfrac{v_{xi}^n+v_{xj}^n}{2}\widetilde{\beta}+\dfrac{u_{yi}^n+u_{yj}^n}{2}\widetilde{\beta}\right) \\ \dfrac{v_{ti}+v_{tj}}{2}\dfrac{h_i^n+h_j^n}{2}\left(\dfrac{v_{xi}^n+v_{xj}^n}{2}\widetilde{\alpha}+\dfrac{u_{yi}^n+u_{yj}^n}{2}\widetilde{\alpha}+2\dfrac{v_{yi}^n+v_{yj}^n}{2}\widetilde{\beta}\right) \end{array}\right\} \tag{19}$$

The eddy viscosities v_{ti} and v_{tj} have no time indices since it has been assumed that these values are constant at each node throughout the hydrodynamic part of the computational process (see Section 6.1). The values $u_{xi}^n, u_{yi}^n, v_{xi}^n, v_{yi}^n$ represent the average of the partial derivatives of u and v, at cell C_i and at time $t=t_n$

$$u_{xi}^n=\left(\overline{\frac{\partial u}{\partial x}}\right)_{C_i,t_n}, \quad u_{yi}^n=\left(\overline{\frac{\partial u}{\partial y}}\right)_{C_i,t_n} \tag{20}$$

$$v_{xi}^n=\left(\overline{\frac{\partial v}{\partial x}}\right)_{C_i,t_n}, \quad v_{yi}^n=\left(\overline{\frac{\partial v}{\partial y}}\right)_{C_i,t_n} \tag{21}$$

These average values are calculated [13] in the same way shown in Section 3.2 for the k–ε variables. Finally, the time step $\Delta t=t_{n+1}-t_n$ is estimated as indicated in [12] as

$$\Delta t\leqslant 0.5\cdot\min\left(\frac{D_{ij}}{(\sqrt{u^2+v^2}+c)_{ij}}\right) \tag{22}$$

where D_{ij} are the distances between each node I and its neighboring nodes, and 0.5 is a coefficient to ensure stability.

Equation (11) provides a time explicit method to calculate the variables, at every node I and at every time step, from the previous time step values at node I and its neighboring nodes. The efficiency of the time integration scheme can be easily raised by using in (11), instead of the Euler-type method, a higher order method (type Runge–Kutta, predictor–corrector, etc.), as shown in [13].

3. THE DEPTH-AVERAGED k–ε MODEL

The coefficient v_t in the turbulent term of the 2D-SWE represents the eddy viscosity of a whole vertical column of fluid. To determine this viscosity different turbulence models can be used. One of them is the well-known k–ε model, in which k and ε are, respectively, the turbulence kinetic energy and the dissipation rate per unit mass. The 2D-SWE are obtained from a depth integration, therefore it seems reasonable to use the two-dimensional depth-averaged version of the k–ε model [26]. In this model, the eddy viscosity is calculated as

$$v_t=c_\mu\frac{k^2}{\varepsilon} \tag{23}$$

DOI: 10.1002/fld

where k and ε are given by the transport equations

$$\frac{\partial k}{\partial t}+u\frac{\partial k}{\partial x}+v\frac{\partial k}{\partial y}=\frac{\partial}{\partial x}\left(\frac{v_t}{\sigma_k}\frac{\partial k}{\partial x}\right)+\frac{\partial}{\partial y}\left(\frac{v_t}{\sigma_k}\frac{\partial k}{\partial y}\right)+P_h+P_{kV}-\varepsilon \tag{24}$$

$$\frac{\partial \varepsilon}{\partial t}+u\frac{\partial \varepsilon}{\partial x}+v\frac{\partial \varepsilon}{\partial y}=\frac{\partial}{\partial x}\left(\frac{v_t}{\sigma_\varepsilon}\frac{\partial \varepsilon}{\partial x}\right)+\frac{\partial}{\partial y}\left(\frac{v_t}{\sigma_\varepsilon}\frac{\partial \varepsilon}{\partial y}\right)+c_{1\varepsilon}\frac{\varepsilon}{k}P_h+P_{\varepsilon V}-c_{2\varepsilon}\frac{\varepsilon^2}{k} \tag{25}$$

being

$$P_h=v_t\left[2\left(\frac{\partial u}{\partial x}\right)^2+2\left(\frac{\partial v}{\partial y}\right)^2+\left(\frac{\partial v}{\partial x}+\frac{\partial u}{\partial y}\right)^2\right] \tag{26}$$

and

$$P_{kV}=\frac{1}{\sqrt{c_f}}\frac{U^{*3}}{h},\quad P_{\varepsilon V}=c_{\varepsilon\Gamma}\frac{c_{2\varepsilon}}{c_f^{3/4}}\sqrt{c_\mu}\frac{U^{*4}}{h^2} \tag{27}$$

P_h is the production of k due to interactions of turbulent stresses with horizontal mean-velocity gradients. P_{kv} and $P_{\varepsilon v}$ are the productions of k and ε due to vertical velocity gradients and are related to the friction velocity U^* (74), which will be calculated from the so-called 'law of the wall' (see Section 5). The friction coefficient c_f can be obtained as

$$c_f=\frac{U^{*2}}{U^2} \tag{28}$$

being $U=\sqrt{u^2+v^2}$.

For wide laboratory flumes, Rastogi *et al.* [15] adopted the value $c_{\varepsilon\Gamma}=3.6$. On the other hand, Nezu *et al.* [27, p. 139] use for $c_{\varepsilon\Gamma}$ the expression $1/\sqrt{v^*}$, being v^* the dimensionless depth-averaged eddy viscosity. Taking the Prandtl–Schmidt number in the range $\sigma_t=0.5$–0.7, they relate the parameter v^* to the dimensionless diffusivity e^* by

$$v^*=e^*\sigma_t \tag{29}$$

and this relationship has been used in our work. The empirical parameter e^* may be measured from dye-spreading experiments. According to Fischer *et al.* [28, p. 112], the values of e^* in straight uniform channels are generally in the range of 0.1–0.2; for natural streams with gradual bends and moderate sidewall irregularities the coefficient lies in the range of 0.4–0.8 and it can increase with sharp bends or rapid changes in geometry. In the case presented in Section 6, with a sudden change in geometry but with a very smooth surface, a value of $e^*=0.6$ has been chosen. As for σ_t, Nezu *et al.* [27] state that the value $e^*=0.15$ has been observed for laboratory flumes. Then we have adopted for σ_t the value 0.5144 which, introduced together with $e^*=0.15$ in Nezu *et al.* formula, results in the value of $c_{\varepsilon\Gamma}=3.6$, taken in [15] for laboratory flumes.

The coefficients $c_\mu, c_{1\varepsilon}, c_{2\varepsilon}, \sigma_k, \sigma_\varepsilon$ are empirical. For the first three of them the standard values [26] have been taken. With regards to σ_k and σ_ε, the proposal of Nezu and Nakagawa has been followed. They state [27, p. 138] that the standard values of [26] were initially obtained by Launder and Spalding [16] taking $\kappa=0.435$ for the Von Karman constant and they propose to give the value 1.2 to both constants if the usual value of 0.41 is taken for κ. The values used in the present work are shown in Table I.

DOI: 10.1002/fld

Table I. Constant coefficients in the depth-averaged k–ε model.

c_μ	$c_{1\varepsilon}$	$c_{2\varepsilon}$	σ_k	σ_ε
0.09	1.44	1.92	1.2	1.2

3.1. Conservative form of the k–ε equations

To express the k–ε equations in conservative form, we shall use the continuity equation

$$\frac{\partial h}{\partial t}+\frac{\partial hu}{\partial x}+\frac{\partial hv}{\partial y}=0 \tag{30}$$

Let us add equation (30) multiplied by k to equation (24) multiplied by h, and equation (30) multiplied by ε to equation (25) multiplied by h. We obtain

$$\frac{\partial (hk)}{\partial t}+\frac{\partial (hku)}{\partial x}+\frac{\partial (hkv)}{\partial y}=hS_1' \tag{31}$$

$$\frac{\partial (h\varepsilon)}{\partial t}+\frac{\partial (h\varepsilon u)}{\partial x}+\frac{\partial (h\varepsilon v)}{\partial y}=hS_2' \tag{32}$$

where S_1' and S_2' are the source terms of equations (24) and (25), respectively. Equations (31) and (32) represent a system of conservation laws with source term, in conservative form, that can be written in matrix form as

$$\frac{\partial \boldsymbol{\gamma}}{\partial t}+\frac{\partial \mathbf{H_1}}{\partial x}+\frac{\partial \mathbf{H_2}}{\partial y}=\mathbf{S} \tag{33}$$

being

$$\boldsymbol{\gamma}=\begin{pmatrix} hk \\ h\varepsilon \end{pmatrix},\quad \mathbf{H_1}=\begin{pmatrix} hku \\ h\varepsilon u \end{pmatrix},\quad \mathbf{H_2}=\begin{pmatrix} hkv \\ h\varepsilon v \end{pmatrix},\quad \mathbf{S}=\begin{pmatrix} hS_1' \\ hS_2' \end{pmatrix} \tag{34}$$

As we shall see in Section 6.1, during the calculation of v_t, the values of h, u, v are assumed to be constant and k, ε are obtained in an iterative process. We have modified, then, the P_h source term to separate v_t from the spatial derivatives of u and v. In this way, P_h is written as $v_t P_{hs}$ and the two components of the source term become

$$S_1=h\left[\frac{\partial}{\partial x}\left(\frac{v_t}{\sigma_k}\frac{\partial k}{\partial x}\right)+\frac{\partial}{\partial y}\left(\frac{v_t}{\sigma_k}\frac{\partial k}{\partial y}\right)+v_t P_{hs}+P_{kV}-\varepsilon\right] \tag{35}$$

$$S_2=h\left[\frac{\partial}{\partial x}\left(\frac{v_t}{\sigma_\varepsilon}\frac{\partial \varepsilon}{\partial x}\right)+\frac{\partial}{\partial y}\left(\frac{v_t}{\sigma_\varepsilon}\frac{\partial \varepsilon}{\partial y}\right)+c_{1\varepsilon}c_\mu k P_{hs}+P_{\varepsilon V}-c_{2\varepsilon}\frac{\varepsilon^2}{k}\right] \tag{36}$$

3.2. Discretization of the k–ε equations

In Section 2.3, the finite volume mesh was described and the FVM was applied to the 2D-SWE, by using the upwind Van Leer Q-scheme. As it will be shown, the k–ε system has two real eigenvalues,

DOI: 10.1002/fld

what suggested us to apply the same method when discretizing the k–ε equations. The method has been successfully used, although references of its application to the depth-averaged k–ε equations are not common in literature.

Using the ∇ operator, the integral in every cell of the k–ε system in conservative form (33) can be expressed as

$$\iint_{C_i} \frac{\partial \boldsymbol{\gamma}}{\partial t}\,\mathrm{d}A + \iint_{C_i} \nabla\cdot\mathscr{H}\,\mathrm{d}A = \iint_{C_i} \mathbf{S}\,\mathrm{d}A, \quad \mathscr{H} = (\mathbf{H_1}, \mathbf{H_2}) \tag{37}$$

Applying the Gauss theorem to the second term, it yields

$$\iint_{C_i} \frac{\partial \boldsymbol{\gamma}}{\partial t}\,\mathrm{d}A + \int_{\Gamma_i} \mathscr{H}\cdot\tilde{\boldsymbol{\eta}}\,\mathrm{d}l = \iint_{C_i} \mathbf{S}\,\mathrm{d}A \tag{38}$$

In the following discretizations of the flux and source terms, the hydrodynamic variables have no time indices since they are assumed to be constant at each node throughout the turbulent part of the computational process (see Section 6.1).

3.2.1. Time derivative. The solution of (33) is now replaced by some values $\boldsymbol{\gamma}_i^n$, constant within each cell C_i and at each time step t_n. The time derivative is discretized by the Forward Euler's method as

$$\left.\frac{\partial \boldsymbol{\gamma}}{\partial t}\right|_{C_i,t_n} \approx \frac{\boldsymbol{\gamma}_i^{n+1} - \boldsymbol{\gamma}_i^n}{\Delta t} \tag{39}$$

whose value is constant over C_i and can be taken out of the corresponding integral in (38).

3.2.2. Flux term. In the second term of (38), the boundary Γ_i is split into a sum of cell interfaces $\Gamma_{ij},\ j \in \mathscr{K}_i$

$$\int_{\Gamma_i} \mathscr{H}\cdot\tilde{\boldsymbol{\eta}}\,\mathrm{d}l = \sum_{j\in\mathscr{K}_i} \int_{\Gamma_{ij}} \mathscr{H}\cdot\tilde{\boldsymbol{\eta}}\,\mathrm{d}l \tag{40}$$

The scalar product $\mathbf{Z_v} = \mathscr{H}\cdot\tilde{\boldsymbol{\eta}}$ at Γ_{ij} is now upwinded, as in the hydrodynamic process, by taking the mean value of $\mathbf{Z_v}$ at nodes I and J plus an upwinding term as the flux through Γ_{ij}. The expression of the numerical flux is

$$\boldsymbol{\phi}_{vij}^n = \frac{\mathbf{Z_v}(\boldsymbol{\gamma}_i^n, \tilde{\boldsymbol{\eta}}_{ij}) + \mathbf{Z_v}(\boldsymbol{\gamma}_j^n, \tilde{\boldsymbol{\eta}}_{ij})}{2} - \frac{1}{2}|\mathbf{Q}_v(\mathbf{U}_Q, \tilde{\boldsymbol{\eta}}_{ij})|(\boldsymbol{\gamma}_j^n - \boldsymbol{\gamma}_i^n) \tag{41}$$

being in this case

$$\mathbf{Q}_v = \tilde{\alpha}\frac{\mathrm{d}\mathbf{H_1}}{\mathrm{d}\boldsymbol{\gamma}} + \tilde{\beta}\frac{\mathrm{d}\mathbf{H_2}}{\mathrm{d}\boldsymbol{\gamma}} = \tilde{\alpha}\begin{pmatrix} u & 0 \\ 0 & u \end{pmatrix} + \tilde{\beta}\begin{pmatrix} v & 0 \\ 0 & v \end{pmatrix} = \begin{pmatrix} \lambda & 0 \\ 0 & \lambda \end{pmatrix} \tag{42}$$

The eigenvalues of $\mathbf{Q}_v$, $\lambda = \tilde{\alpha}u + \tilde{\beta}v$, represent the projection of the velocity vector over the normal to the edge; they are positive if the fluid enters the cell and negative if the fluid goes out. Its value is zero if the velocity is parallel to the edge. Matrix $|\mathbf{Q}|_v$ is defined as in (14)

$$|\mathbf{Q}|_v = \mathbf{X}_v|\boldsymbol{\Lambda}|_v\mathbf{X}_v^{-1} \tag{43}$$

DOI: 10.1002/fld

being $\mathbf{X}_v$ the eigenvectors matrix of $\mathbf{Q}_v$. As $|\mathbf{\Lambda}|_v = |\lambda|\mathbf{I}$ ($\mathbf{I}$ is the identity matrix), $|\mathbf{Q}|_v$ becomes

$$|\mathbf{Q}|_v = \begin{pmatrix} |\lambda| & 0 \\ 0 & |\lambda| \end{pmatrix} \tag{44}$$

and it is evaluated at $\mathbf{U}_Q$ (15).

We are trying to calculate the flux $\mathbf{Z}_v$ through the edge Γ_{ij}, from the values of the variables $hk, h\varepsilon$ at the nodes I and J. Now, if we take for u and v their values at U_Q when calculating the flux at I and at J, these fluxes become

$$\mathbf{Z}_{vi} = \begin{Bmatrix} h_i\, k_i^n \lambda_Q \\ h_i\, \varepsilon_i^n \lambda_Q \end{Bmatrix}, \quad \mathbf{Z}_{vj} = \begin{Bmatrix} h_j\, k_j^n \lambda_Q \\ h_j\, \varepsilon_j^n \lambda_Q \end{Bmatrix} \tag{45}$$

If $\lambda_Q > 0$

$$|\lambda_Q| = \lambda_Q \implies \boldsymbol{\phi}_{vij}^n = \begin{Bmatrix} h_i\, k_i^n \lambda_Q \\ h_i\, \varepsilon_i^n \lambda_Q \end{Bmatrix} = \mathbf{Z}_{vi} \tag{46}$$

and if $\lambda_Q < 0$

$$|\lambda_Q| = -\lambda_Q \implies \boldsymbol{\phi}_{vij}^n = \begin{Bmatrix} h_j\, k_j^n \lambda_Q \\ h_j\, \varepsilon_j^n \lambda_Q \end{Bmatrix} = \mathbf{Z}_{vj} \tag{47}$$

Otherwise

$$\lambda_Q = 0 \implies \boldsymbol{\phi}_{vij}^n = 0 \tag{48}$$

This result greatly simplifies expression (41) and gives a graphic interpretation of the upwinding. If the fluid enters the cell, the value of the variables hk and $h\varepsilon$ at Γ_{ij} is their value at node J, from which the flow comes. If the fluid goes out, the value at node I is taken.

3.2.3. Source term. To discretize the source term, an intermediate state $\boldsymbol{\gamma}_Q$ is defined by

$$k_Q^n = \frac{h_i\, k_i^n + h_j\, k_j^n}{h_i + h_j}, \quad \varepsilon_Q^n = \frac{h_i\, \varepsilon_i^n + h_j\, \varepsilon_j^n}{h_i + h_j}, \quad {v_t}_Q^n = \frac{v_{ti}^n + v_{tj}^n}{2} \tag{49}$$

where only k and ε have time indices (see Section 6.1). Now the source term is split into two parts, to treat them separately

$$\mathbf{S}_L = \begin{Bmatrix} h\dfrac{\partial}{\partial x}\left(\dfrac{v_t}{\sigma_k}\dfrac{\partial k}{\partial x}\right) + h\dfrac{\partial}{\partial y}\left(\dfrac{v_t}{\sigma_k}\dfrac{\partial k}{\partial y}\right) \\ h\dfrac{\partial}{\partial x}\left(\dfrac{v_t}{\sigma_\varepsilon}\dfrac{\partial \varepsilon}{\partial x}\right) + h\dfrac{\partial}{\partial y}\left(\dfrac{v_t}{\sigma_\varepsilon}\dfrac{\partial \varepsilon}{\partial y}\right) \end{Bmatrix} \tag{50}$$

$$\mathbf{S}_R = \begin{Bmatrix} h\,(v_t P_{hs} + P_{kV} - \varepsilon) \\ h\left(c_{1\varepsilon} c_\mu k P_{hs} + P_{\varepsilon V} - c_{2\varepsilon}\dfrac{\varepsilon^2}{k}\right) \end{Bmatrix} \tag{51}$$

DOI: 10.1002/fld

To discretize the integral of $\mathbf{S}_L$, h is replaced by its value at node I, the Gauss theorem is applied and the boundary Γ_i is split into a sum of cell interfaces as in (40). Using the ∇ operator it results in

$$\iint_{C_i} \mathbf{S}_L \,\mathrm{d}A \approx \begin{Bmatrix} h_i \sum\limits_{j\in\mathscr{K}_i} \int_{\Gamma_{ij}} \dfrac{\nu_t}{\sigma_k} \nabla k \cdot \widetilde{\boldsymbol{\eta}} \,\mathrm{d}l \\ h_i \sum\limits_{j\in\mathscr{K}_i} \int_{\Gamma_{ij}} \dfrac{\nu_t}{\sigma_\varepsilon} \nabla \varepsilon \cdot \widetilde{\boldsymbol{\eta}} \,\mathrm{d}l \end{Bmatrix} \tag{52}$$

At equation (52) we need to estimate, at every Γ_{ij}, the escalar product

$$\nabla k \cdot \widetilde{\boldsymbol{\eta}} = \widetilde{\alpha} \frac{\partial k}{\partial x} + \widetilde{\beta} \frac{\partial k}{\partial y} \tag{53}$$

Two methods for calculating the partial derivatives of u and v at the edge between two cells have been described and compared in [13], where the better performance of the one that uses the average values of the derivatives at cells C_i and C_j has been concluded. Next the partial derivatives of k and ε at Γ_{ij} are obtained by applying the same method.

Thus, to approximate the gradient at Γ_{ij} of a scalar magnitude m, the mean value of its gradients at cells C_i and C_j is used. The gradient of m within C_i is estimated as

$$(\overline{\nabla m})_{C_i} = \frac{1}{A_i} \iint_{C_i} \nabla m \,\mathrm{d}A \tag{54}$$

and the surface integral of ∇m over C_i is calculated as [29]

$$\iint_{C_i} \nabla m \,\mathrm{d}A = \int_{\Gamma_i} m \widetilde{\boldsymbol{\eta}} \,\mathrm{d}l \tag{55}$$

being $\widetilde{\boldsymbol{\eta}}$ the unit vector normal to Γ_i. Since

$$\widetilde{\boldsymbol{\eta}} = \widetilde{\alpha}\mathbf{i} + \widetilde{\beta}\mathbf{j} \tag{56}$$

and

$$(\overline{\nabla m})_{C_i} = \left(\overline{\frac{\partial m}{\partial x}}\right)_{C_i} \mathbf{i} + \left(\overline{\frac{\partial m}{\partial y}}\right)_{C_i} \mathbf{j} \tag{57}$$

where $\mathbf{i}$ is the x-axis unit vector and i is the cell index, the average values of the partial derivatives of m within C_i become

$$\left(\overline{\frac{\partial m}{\partial x}}\right)_{C_i} = \frac{1}{A_i} \int_{\Gamma_i} m \widetilde{\alpha} \,\mathrm{d}l = \frac{1}{A_i} \sum_{j\in\mathscr{K}_i} \int_{\Gamma_{ij}} m \widetilde{\alpha} \,\mathrm{d}l \tag{58}$$

$$\left(\overline{\frac{\partial m}{\partial y}}\right)_{C_i} = \frac{1}{A_i} \int_{\Gamma_i} m \widetilde{\beta} \,\mathrm{d}l = \frac{1}{A_i} \sum_{j\in\mathscr{K}_i} \int_{\Gamma_{ij}} m \widetilde{\beta} \,\mathrm{d}l \tag{59}$$

DOI: 10.1002/fld

Then the process is summarized as follows. First, the values of k and ε at Γ_{ij} are estimated as their mean values at nodes I and J. Then the partial derivatives of k and ε within every cell C_i are obtained from the estimated values of k and ε at Γ_{ij} by

$$\left(\overline{\frac{\partial k}{\partial x}}\right)_{C_i} = \frac{1}{A_i}\sum_{j\in\mathscr{K}_i}\frac{k_i+k_j}{2}\widetilde{\alpha}\|\boldsymbol{\eta}_{ij}\|, \quad \left(\overline{\frac{\partial \varepsilon}{\partial x}}\right)_{C_i} = \frac{1}{A_i}\sum_{j\in\mathscr{K}_i}\frac{\varepsilon_i+\varepsilon_j}{2}\widetilde{\alpha}\|\boldsymbol{\eta}_{ij}\| \tag{60}$$

$$\left(\overline{\frac{\partial k}{\partial y}}\right)_{C_i} = \frac{1}{A_i}\sum_{j\in\mathscr{K}_i}\frac{k_i+k_j}{2}\widetilde{\beta}\|\boldsymbol{\eta}_{ij}\|, \quad \left(\overline{\frac{\partial \varepsilon}{\partial y}}\right)_{C_i} = \frac{1}{A_i}\sum_{j\in\mathscr{K}_i}\frac{\varepsilon_i+\varepsilon_j}{2}\widetilde{\beta}\|\boldsymbol{\eta}_{ij}\| \tag{61}$$

and we can obtain the value of the partial derivatives at Γ_{ij} from the corresponding values of the derivatives at C_i and C_j. By expressing the average values within C_i at time $t=t_n$ as

$$k_{xi}^n = \left(\overline{\frac{\partial k}{\partial x}}\right)_{C_i,t_n}, \quad \varepsilon_{xi}^n = \left(\overline{\frac{\partial \varepsilon}{\partial x}}\right)_{C_i,t_n} \tag{62}$$

$$k_{yi}^n = \left(\overline{\frac{\partial k}{\partial y}}\right)_{C_i,t_n}, \quad \varepsilon_{yi}^n = \left(\overline{\frac{\partial \varepsilon}{\partial y}}\right)_{C_i,t_n} \tag{63}$$

and by taking the values of ν_t corresponding to $\boldsymbol{\gamma}_Q$, the discretized integral of $\mathbf{S}_L$ at Γ_{ij} and at $t=t_n$ is

$$\widehat{\mathbf{S}}_{Lij}^n = \begin{Bmatrix} h_i\dfrac{\nu_{tQ}^n}{\sigma_k}\left(\dfrac{k_{xi}^n+k_{xj}^n}{2}\widetilde{\alpha}+\dfrac{k_{yi}^n+k_{yj}^n}{2}\widetilde{\beta}\right) \\ h_i\dfrac{\nu_{tQ}^n}{\sigma_\varepsilon}\left(\dfrac{\varepsilon_{xi}^n+\varepsilon_{xj}^n}{2}\widetilde{\alpha}+\dfrac{\varepsilon_{yi}^n+\varepsilon_{yj}^n}{2}\widetilde{\beta}\right) \end{Bmatrix} \tag{64}$$

To discretize the integral of $\mathbf{S}_R$ in an analogous way, h is calculated at I and the rest of the variables are calculated at the intermediate states $\mathbf{U}_Q$ (for u, v) and $\boldsymbol{\gamma}_Q$ (for k, ε). This results in

$$\widehat{\mathbf{S}}_{Rij}^n = \begin{Bmatrix} h_i(\nu_{tQ}^n(P_{hs})_Q+(P_{kV})_Q-\varepsilon_Q^n) \\ h_i\left(c_{1\varepsilon}c_\mu k_Q^n(P_{hs})_Q+(P_{\varepsilon V})_Q-c_{2\varepsilon}\left(\dfrac{\varepsilon^2}{k}\right)_Q^n\right) \end{Bmatrix} \tag{65}$$

Finally, the surface integral within C_i of the source term of (38) is approximated as

$$\iint_{C_i}\mathbf{S}\,\mathrm{d}A \approx \sum_{j\in\mathscr{K}_i}(\|\boldsymbol{\eta}_{ij}\|\widehat{\mathbf{S}}_{Lij}^n + A_{ij}\widehat{\mathbf{S}}_{Rij}^n) \tag{66}$$

3.2.4. Algorithm. Using the above described method, a discretization of equation (38) has been obtained, which takes the form

$$\frac{\boldsymbol{\gamma}_i^{n+1}-\boldsymbol{\gamma}_i^n}{\Delta t}A_i + \sum_{j\in\mathscr{K}_i}\|\boldsymbol{\eta}_{ij}\|\boldsymbol{\phi}_{vij}^n = \sum_{j\in\mathscr{K}_i}(\|\boldsymbol{\eta}_{ij}\|\widehat{\mathbf{S}}_{Lij}^n + A_{ij}\widehat{\mathbf{S}}_{Rij}^n) \tag{67}$$

DOI: 10.1002/fld

Therefore

$$\gamma_i^{n+1}=\gamma_i^n+\frac{\Delta t}{A_i}\left(\sum_{j\in\mathscr{K}_i}(\|\boldsymbol{\eta}_{ij}\|\widehat{\mathbf{S}}_{Lij}^n+A_{ij}\widehat{\mathbf{S}}_{Rij}^n)-\sum_{j\in\mathscr{K}_i}\|\boldsymbol{\eta}_{ij}\|\boldsymbol{\phi}_{vij}^n\right) \tag{68}$$

4. AN ALTERNATIVE: THE q–r MODEL

Both the turbulent kinetic energy and the dissipation rate are non-negative variables. If equations k–ε are discretized directly, negative values can arise, which would produce numerical problems, besides representing a non-physical value for these variables. A way to avoid this problem is the change of variables used by [30] in a finite element context

$$k=q^2,\quad \varepsilon=r^2 \tag{69}$$

To obtain the q–r equations in conservative form, substitution (69) is used in expressions (24)–(25). Then, after differentiating q^2 and r^2 in the left-hand side terms, the process described in Section 3.1 is repeated. Thus we obtain

$$\frac{\partial\boldsymbol{\gamma}^*}{\partial t}+\frac{\partial\mathbf{H}_1^*}{\partial x}+\frac{\partial\mathbf{H}_2^*}{\partial y}=\mathbf{S}^* \tag{70}$$

As it can be seen, the above stated equations take the same form of system (33), now being

$$\boldsymbol{\gamma}^*=\begin{pmatrix}hq\\hr\end{pmatrix},\quad \mathbf{H}_1^*=\begin{pmatrix}hqu\\hru\end{pmatrix},\quad \mathbf{H}_2^*=\begin{pmatrix}hqv\\hrv\end{pmatrix},\quad \mathbf{S}^*=\begin{pmatrix}S_1^*\\S_2^*\end{pmatrix} \tag{71}$$

with

$$S_1^*=\frac{h}{2q}\left[\frac{\partial}{\partial x}\left(\frac{v_t 2q}{\sigma_k}\frac{\partial q}{\partial x}\right)+\frac{\partial}{\partial y}\left(\frac{v_t 2q}{\sigma_k}\frac{\partial q}{\partial y}\right)+v_t P_{hs}+P_{kV}-r^2\right] \tag{72}$$

$$S_2^*=\frac{h}{2r}\left[\frac{\partial}{\partial x}\left(\frac{v_t 2r}{\sigma_\varepsilon}\frac{\partial r}{\partial x}\right)+\frac{\partial}{\partial y}\left(\frac{v_t 2r}{\sigma_\varepsilon}\frac{\partial r}{\partial y}\right)+c_{1\varepsilon}c_\mu q^2 P_{hs}+P_{\varepsilon V}-c_{2\varepsilon}\frac{r^4}{q^2}\right] \tag{73}$$

These source terms have the same form of expressions (35)–(36), where (k,ε) are replaced by (q^2,r^2) and the two components are multiplied by $1/2q$ and by $1/2r$, respectively. Therefore, the discretization process of the q–r equations is analogous to that of the k–ε equations.

5. BOUNDARY CONDITIONS

5.1. Calculation of the friction velocity

The friction velocity is defined [31, p. 14] in terms of the wall stress τ_w and of the density ρ as

$$U^*=\sqrt{\frac{\tau_w}{\rho}} \tag{74}$$

DOI: 10.1002/fld

It has many applications such as the obtaining of the production terms (27) as well as the calculation of the dimensionless velocity U^+ and of the wall distance y^+, being

$$U^+ = \frac{U}{U^*}, \quad y^+ = \frac{y U^*}{v} \tag{75}$$

U is the velocity component parallel to the wall, y is the normal distance to the wall and v is the fluid viscosity. In the vicinity of the wall, the relationship between U^+ and y^+ can be described approximately by the law of the wall that reads

$$U^+ = \frac{1}{\kappa} \ln(E y^+), \quad 30 < y^+ < 500 \tag{76}$$

where the Von Karman constant takes the usual value $\kappa = 0.41$ and $E = 9.8$ [32, p. 60]. The range of validity for the law of the wall varies among the authors [26, 27, 31, 32]. The one proposed by [32] has been used here.

To obtain the value of U^* an iteration is made, once the distance y and the fluid velocity U have been chosen. These values must be carefully selected, so that the value of y^+ resulting from U^* lies within the range of validity in most of the nodes. In our calculations, the velocity component parallel to the boundary has been taken for U. The distance y has been estimated in order to fulfil the range condition, resulting in a value of $y = 0.022$, about 0.8Δ (Δ is the average mesh size at the boundary). Taking expressions (75) for y^+ and U^+ and rearranging, the law of the wall can be rewritten as

$$U^* = \frac{U\kappa}{\ln\left(\dfrac{E y U^*}{v}\right)} \tag{77}$$

Then the iteration can be made by successive approximations, yielding the value of U^*. The use of the Newton Raphson's method has been of utility to greatly accelerate the convergence.

On the other hand, Spalding [33] (also reported in [34, 35]) obtained an alternative expression for the law of the wall, based on Taylor series, valid for both the viscous sublayer and the logarithmic zone,

$$y^+ = U^+ + \mathrm{e}^{-\kappa B}\left[\mathrm{e}^{\kappa U^+} - 1 - \kappa U^+ - \frac{(\kappa U^+)^2}{2} - \frac{(\kappa U^+)^3}{6}\right] \tag{78}$$

being $B = 5.0$. This formula has also been used in our calculations. Eliminating U^* from (75), we have

$$U^+ = \frac{U y}{v y^+} \tag{79}$$

and the iteration can be made, what yields the value of U^+, from which U^* can be calculated. In this case the use of Newton Raphson's method has been necessary to achieve convergence, since the successive approximations iteration is divergent. The values obtained with Spalding's law have been very similar to the ones obtained with the logarithmic law. Therefore, since Spalding's law is valid within a wider range of distances to the wall, it has been the one chosen for our work.

DOI: 10.1002/fld

5.2. Hydrodynamic process. Wall conditions in channels

At inlet and outlet sections the usual conditions for the hydrodynamic equations are applied. If the flow is subcritical, the discharge at the inlet and the depth at the outlet must be imposed. In order to account for the stress at the nodes on the wall, the following four conditions, characterized by a wall index I_w, have been considered.

(a) No-slip condition ($I_w=0$). The velocity at the wall nodes is set to zero. This condition corresponds strictly to the physical problem, since the fluid particles at the wall are stopped by it, transmitting to the neighboring ones the effect of the wall. To properly apply this condition a very fine mesh near the wall would be needed, so as not to distort excessively the velocity field, and this would make the solution computationally expensive. The no-slip condition is usually employed when studying the cavity flow problem.

(b) Slip condition ($I_w=1$). The velocity component normal to the wall is set to zero. It is a useful condition when friction at the wall has not to be accounted for, as it is the case in many one-dimensional problems.

(c) Friction condition ($I_w=2$). The velocity component normal to the wall is set to zero and the friction effect of the wall is considered by using the following expression [29] for the hydraulic radius

$$R_h=\frac{A_b h}{A_b+A_w}=\frac{h}{1+A_w/A_b} \tag{80}$$

where A_b represents the cell area and A_w the wall area corresponding to the cell (see Figure 3). In this way the value of the hydraulic radius is reduced according to the importance of the lateral surface with respect to the bottom surface, thus increasing the friction terms S_{fx} and S_{fy} (5). Brufau *et al.* [12] have proposed another expression to take into account the side walls effect with the possibility of giving different values to Manning's coefficient at the walls and the bottom.

(d) Friction velocity condition ($I_w=3$). The velocity component normal to the wall is set to zero and the stress at the wall is calculated from (74) as

$$\boldsymbol{\tau}_w=-\rho U^{*2}\mathbf{t} \tag{81}$$

being $\mathbf{t}$ the unit vector tangent to the boundary in the flow direction.

To compare the four above described conditions, some measurements were made at the Hydraulics Laboratory of the Civil Engineering School of A Coruña. The installation was a model of a channel 0.5 m wide, with a length of about 3.8 m. This model reproduced a real channel existing at the power station of As Pontes de García Rodríguez (A Coruña, Spain). After a bend the channel splits into three different branches (clockwise numerated as 1, 2, 3) each one having a step 0.123 m high. The triangular mesh, with 3423 nodes, was generated by using a commercial code [36]. The size of the triangles sides is about 3 cm long. The imposed conditions in the numerical simulation were: at the inlet, a discharge of 42.4 l/s and, at the three outlets, the measured depth of 0.1 m. The bottom friction effect was estimated by Manning's formula in the four cases. The initial conditions were: fluid at rest and a horizontal free surface, determined by the fixed depth of 0.1 m after the step. The velocity field and streamlines are depicted in Figure 4. Once the steady flow was reached, the depth and velocity field were obtained in the four cases. It was observed that the discharges at the three outlets varied significantly with the wall condition

DOI: 10.1002/fld

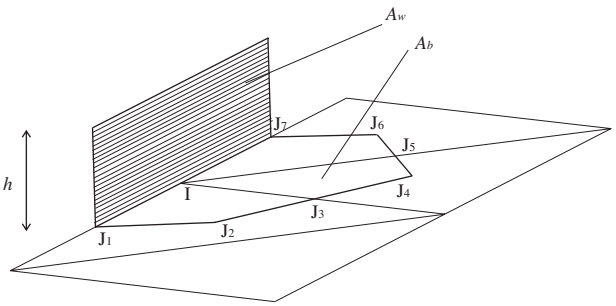

Figure 3. Wet wall area in a boundary cell.

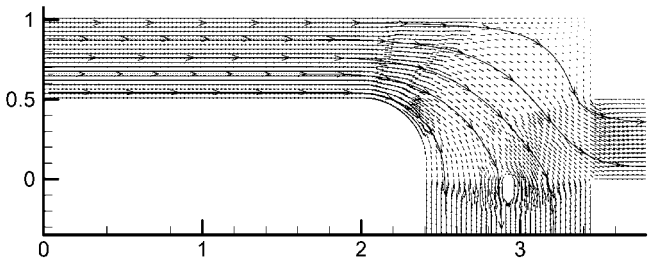

Figure 4. As Pontes channel. Velocity field.

Table II. Comparison of wall conditions. Discharges in l/s.

	Measured discharges Q_{mi}	Computed discharges Q_{ci}			
		$I_w=0$	$I_w=1$	$I_w=2$	$I_w=3$
Outlet 1	13.27	16.24	13.51	13.66	13.68
Outlet 2	14.84	15.14	14.98	15.08	14.77
Outlet 3	14.24	10.83	13.25	13.69	13.90
$\sum Q_i$	42.35	42.21	41.74	42.43	42.35
σ	—	2.616	0.594	0.413	0.310

employed. The computed results Q_{ci} and the experimental measures Q_{mi} are shown in Table II. The sum of the three partial discharges and the deviation

$$\sigma=\sqrt{\sum_{n=1}^{3}\frac{(Q_{ci}-Q_{mi})^2}{3}} \tag{82}$$

of the computed discharges with respect to the measured ones are also presented. The closest results to the measures were obtained for $I_w=3$. This has been the wall condition applied in Section 6.

DOI: 10.1002/fld

5.3. k–ε process. Boundary conditions in channels

5.3.1. Inlet condition. The amount of turbulence that enters the domain depends on the processes previously underwent through by the fluid. The most adequate inlet condition would be of Dirichlet-type, measuring k experimentally and obtaining ε from other turbulent quantities. Usually these values are not known and have to be estimated, while the computational domain must be extended to get the zone of interest away from the inlet, in order to minimize its influence. Fortunately this influence is not strong [37], specially when a great amount of turbulence is generated inside the domain. Nezu and Nakagawa [27, pp. 54, 77] propose, for the vertical distribution of k and ε far from the walls in a laboratory channel, the following expressions

$$k(z)=4.78U^{*2}\mathrm{e}^{-2z/h}, \quad \varepsilon(z)=E_1\frac{U^{*3}}{h}\sqrt{\frac{h}{z}}\,\mathrm{e}^{-3z/h} \tag{83}$$

with $E_1=9.8$ for Re between 10^4 and 10^5. Depth-averaging the first expression we obtain

$$k=\frac{1}{h}\int_0^h k(z)\,\mathrm{d}z=4.78\,U^{*2}\,\frac{\mathrm{e}^2-1}{2\mathrm{e}^2}=2.06655U^{*2} \tag{84}$$

The expression for $\varepsilon(z)$ has no primitive and has to be calculated numerically, yielding

$$\varepsilon=\frac{1}{h}\int_0^h \varepsilon(z)\,\mathrm{d}z=\frac{E_1U^{*3}}{h}\int_0^h\frac{\mathrm{e}^{-3z/h}}{h\sqrt{z/h}}\,\mathrm{d}z=1.008687\frac{E_1U^{*3}}{h} \tag{85}$$

These expressions can also be used to estimate the initial values unless other more adequate values are available (e.g. results from a previous calculation).

5.3.2. Wall and outlet condition. Conditions very common in the literature [26, 27, 32, 38] have been adopted. They are of Dirichlet-type at the walls

$$k=\frac{U^{*2}}{\sqrt{c_\mu}}, \quad \varepsilon=\frac{U^{*3}}{\kappa y} \tag{86}$$

and of Neumann-type at the outlet

$$\frac{\partial k}{\partial n}=\nabla k\cdot\mathbf{n}=0, \quad \frac{\partial \varepsilon}{\partial n}=\nabla\varepsilon\cdot\mathbf{n}=0 \tag{87}$$

where n and $\mathbf{n}$ represent the outward normal direction and the unit vector, respectively.

6. EXPERIMENTAL VALIDATION

6.1. Separation of hydrodynamic and turbulent processes

Both the 2D-SWE and the k–ε system are composed of transport equations and have the same structure, but they represent different phenomena with different time scales and variables. Besides, the k–ε equations have a number of empirical coefficients, some of them problem-dependent.

For these reasons we have proceeded cyclically, as it is suggested in [39, p. 269]. With an initial uniform value for the viscosity, the distribution of velocities and depths is calculated in an

DOI: 10.1002/fld

iterative process (hydraulic phase), according to expression (11), until a steady state is reached. Then, starting from the values of u, v and h at every point, the distribution of v_t is obtained, in another iterative process (k–ε phase), according to expression (68). Then, again the distribution of velocities and depths is calculated, and so on. In each phase, the steady state is assumed to be reached when the difference between the values of each variable in two successive time steps is below a certain tolerance. The combination of the k–ε phase and the subsequent hydraulic phase is said to be a cycle. The calculations end when convergence is achieved in the first iteration, in the hydraulic phase of a cycle.

If the initial uniform value for v_t is small, the resulting velocities are high. Therefore, the turbulent viscosities calculated in cycle 2 are also high and the velocities calculated with it are very small. For this reason, in cycle 3, the calculated viscosities are again small what produces a rise in the values of the corresponding velocities, and so on. In this way, oscillations in the levels of viscosity and velocity are produced and the convergence to the steady state is very slow.

A practical method to reduce the number of required cycles is to limit the number of iterations in each phase. The first cycles are stopped without reaching the steady state in any of the phases and the resulting viscosity values are generally smaller than the converged value. However, since these values are properly distributed through the domain, in a few cycles the steady state is reached in both phases. This results in a significant computational saving.

6.2. Measurement of the turbulent kinetic energy

The experimental data were obtained at the Hydraulics Laboratory of the Civil Engineering School of A Coruña with SONTEK Micro Acoustic Doppler Velocimeters that produce a small distortion of the velocity field. They are highly accurate (10^{-3} m/s) and they take between 80 and 250 measures per second. As the output values have a maximum frequency of 50 Hz, every one represents an average of several measures. In our case, 2500 values of the velocity components were obtained at every point, in a period of 100 s. The measures were taken at a distance from the bottom of $z=9.36$ cm, at 368 points.

The system gives the three mean velocities u, v, w and the three standard deviations $\sigma_x, \sigma_y, \sigma_z$. Since the model is two-dimensional we only have taken into account the x and y deviations, what seems more coherent with the previous hypothesis. The experimental measure of the turbulent kinetic energy is then obtained as

$$k=\tfrac{1}{2}(\sigma_x^2+\sigma_y^2) \tag{88}$$

6.3. Description of the installation and boundary conditions

The experimental domain consisted of a horizontal channel made of glass with an abrupt expansion, commonly known as backward facing step. The dimensions can be seen in Figure 5. A numerical mesh of 3321 nodes (Figure 6) was generated [36]. The applied boundary conditions were [40]

- Upstream: The discharge, $Q=20.21$/s, was imposed.
- Downstream: The measured depth, $h=24.2$ cm, was imposed.
- Walls: the condition (81) was applied.

When 2D-SWE are used without the turbulent term, it is assumed that the turbulent energy losses are globally accounted for by means of the friction coefficient. As we do consider turbulent effects, a reduced value of $n=0.008$ was chosen instead of the estimated for the channel, that

DOI: 10.1002/fld

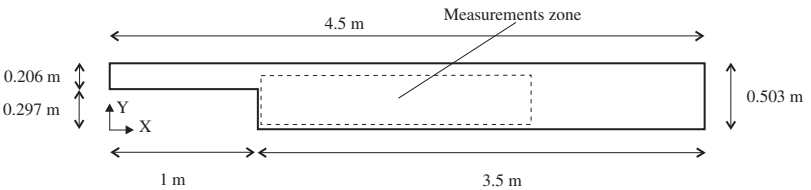

Figure 5. Dimensions of the domain.

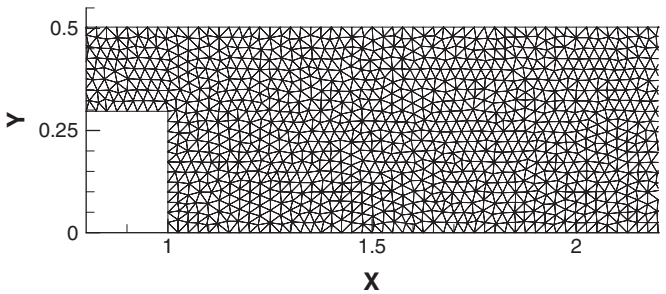

Figure 6. Triangular mesh.

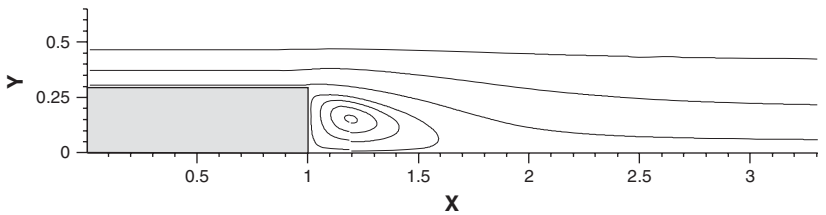

Figure 7. Simplified model. Streamlines. General view.

would be $n = 0.010$–0.012 [41]. In any case, the observed influence of the value of n on the results was very small.

6.4. Results

First the model was applied without taking into account the turbulent term and without reducing the numerical diffusion, by giving a value of 1 to the c_d coefficient in expression (12). The results are shown in Figure 7. We call this the simplified model and it has proved to be reliable in 1D tests [29] but, in the described case, the reattachment length is too short, although the eddy after the step is reproduced.

Then the k–ε and q–r models were used with c_d values of 0.05 and 0.04, respectively. The smaller value of c_d in the q–r model can be used because of the superior numerical stability of this model with respect to the k–ε and it is meant to produce a further reduction in the numerical diffusion. The streamlines obtained with both of them are very similar from each other and close

DOI: 10.1002/fld

to the experimental measures. The q–r results are presented in Figure 8 in a general view. The k–ε results are presented in Figure 9 in an enlarged view, in order to compare them with the experimental results (Figure 10). In Figure 9, only one out of four vectors are plotted, in the x-direction. We notice that these models calculate the reattachment length very accurately, although it has been said [42] that the k–ε model tends to underpredict it by a rate of 20–25%.

The results for k are shown in Figures 11–13. The levels are well predicted by both models, but the position is not so accurately assessed. The zone of maximum values is displaced a little downstream, specially in the k–ε model. The q–r zone for k values over $0.075\,\mathrm{m}^2/\mathrm{s}$ is a little wider than in the experimental measures. Due to the simplifying hypothesis made for the walls, both models fail to reproduce the high k levels near the right wall of the channel.

The q–r model has been implemented to avoid numerical instabilities. In order to compare the efficiency in using the q–r or k–ε models when no instabilities appear, three x-sections of the eddy zone are shown in Figures 14–16. It can be seen that the performance of the simplified model in the presence of eddies is poor. Both the k–ε and q–r models improve significantly the predicted values of u, the first of them giving slightly more accurate results.

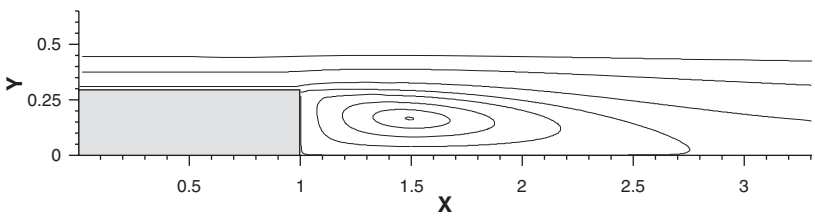

Figure 8. q–r model. Streamlines. General view.

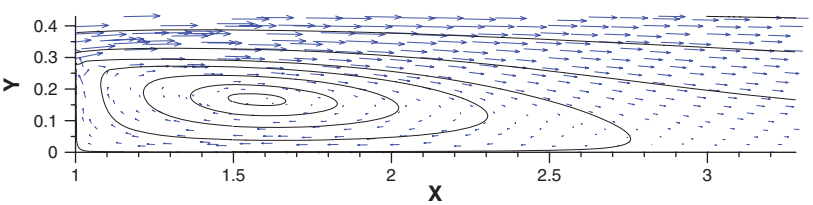

Figure 9. k–ε model. Streamlines and velocity vectors in measurements zone.

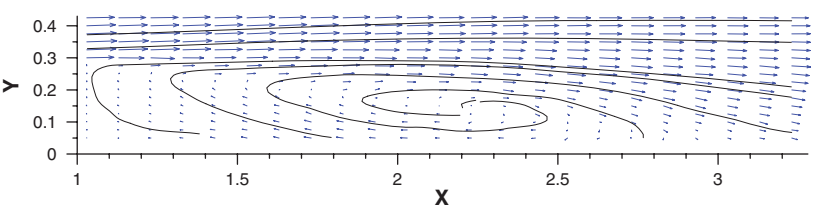

Figure 10. Experimental measures. Streamlines and velocity vectors.

DOI: 10.1002/fld

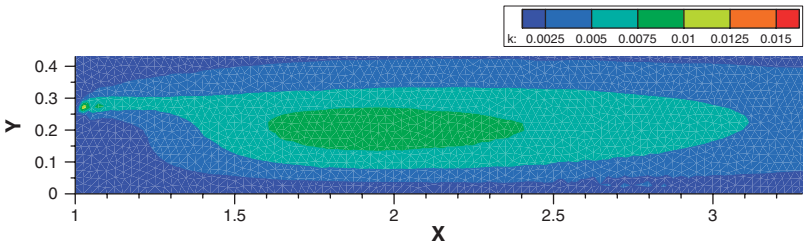

Figure 11. q–r model. Turbulent kinetic energy in measurements zone.

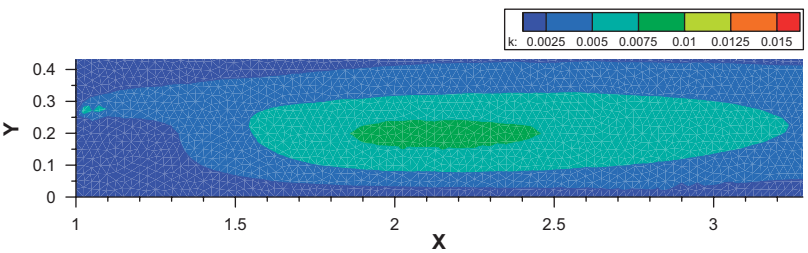

Figure 12. k–ε model. Turbulent kinetic energy in measurements zone.

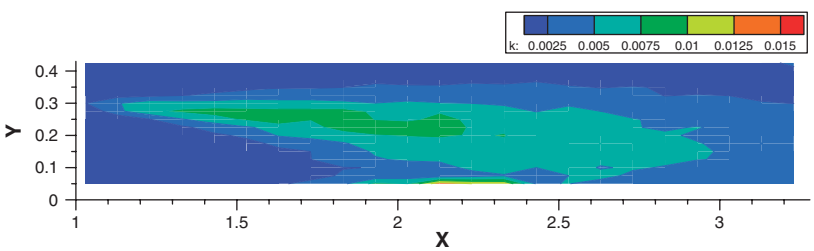

Figure 13. Experimental measures. Turbulent kinetic energy.

This case was computed in 2007 in a Compaq Alpha AXP ES/40 server running True64 Unix with the Compaq FORTRAN 90 compiler. It took about 80 min to complete the analysis. The same analysis can be performed in 2008 in about 13 min, in a departmental server type Dell PowerEdge 2950 with a Intel Xeon 5150 processor and the Intel FORTRAN Compiler for Linux 9.0.

The presented examples were compared with results obtained for an increased level of mesh refinement (12 881 nodes instead of 3321). In our experience, increasing the number of computational nodes was needless, since the results (at the scale of the whole mesh) were not noticeably improved while the computational cost was much higher (about 8 times, what agrees with the theoretical prediction). Thus we conclude that a moderate level of mesh refinement can be sufficient to obtain quite accurate results in practice, with a reasonable computational effort. It seems that increasing the mesh refinement level is only justified when highly accurate results are required for a limited part of the whole domain.

DOI: 10.1002/fld

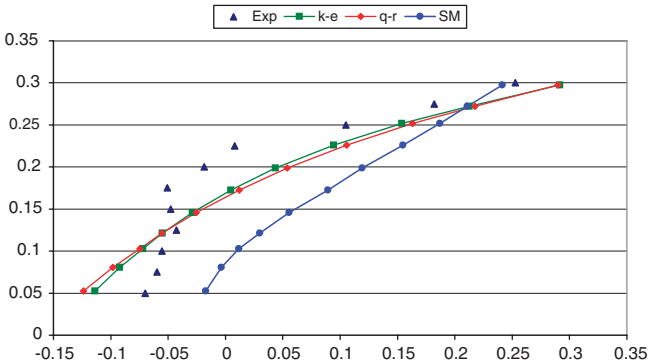

Figure 14. Velocity component u in the eddy zone. Section $x = 1.53$ m.

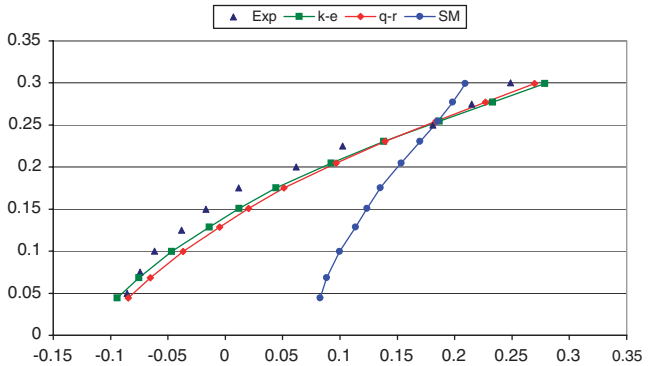

Figure 15. Velocity component u in the eddy zone. Section $x = 2.03$ m.

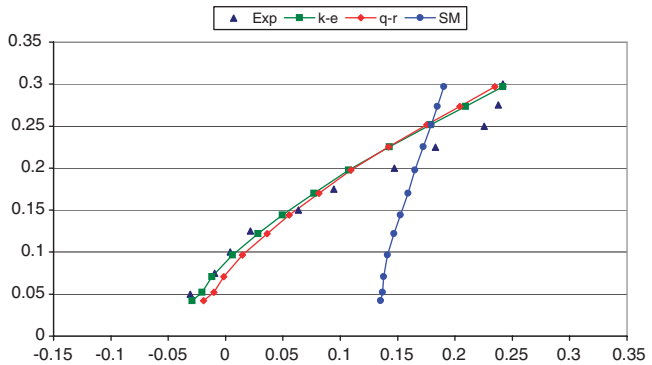

Figure 16. Velocity component u in the eddy zone. Section $x = 2.53$ m.

DOI: 10.1002/fld

7. CONCLUSIONS

Two depth-averaged turbulence models, q–r and k–ε, and their discretization have been described and their performance has been compared with experimental results. Both produce a remarkable improvement with respect to the simplified model (that does not consider the turbulent term) in presence of eddies. The q–r model, developed as a modification of the k–ε to improve stability, has given similar results to the k–ε model in the estimation of the k levels and it has more accurately predicted the position of the maximum values of k. On the other hand, its estimation of the velocity values has been slightly less accurate than the one made by the k–ε model. Both models have correctly calculated the position and length of the eddy.

A comparison of four wall boundary conditions for the hydrodynamic equations has been made, concluding that the better performance corresponds to the one that involves the velocity friction at the wall. An iterative method to calculate the friction velocity with two different formulae is proposed. Two depth-averaged expressions to estimate the k and ε inlet conditions in a channel have been obtained.

The technique herein presented can be applied to both structured and unstructured meshes.

The results, obtained with the proposed first-order models, can be considered very satisfactory. Some improvements could be expected if higher order methods were used, although the computational cost should also be higher.

ACKNOWLEDGEMENTS

This work has been partially supported by Grants #PGIDIT06TAM11801PR and PGIDIT05PXIC 118002PN of the *Xunta de Galicia*, by Grants #DPI2004-05156, DPI2006-15275, and DPI2007-61214 of the *Ministerio de Educación y Ciencia* cofinanced with FEDER funds, and by research fellowships of the *Universidad de A Coruña* and the *Fundación de la Ingeniería Civil de Galicia*.

REFERENCES

1. Vreugdenhil CB. *Numerical Methods for Shallow-water Flow*. Kluwer Academic Publishers: Dordrecht, The Netherlands, 1994.
2. Peña E, Fe J, Puertas J, Sánchez-Tembleque F, Cea L. Experimental validation of a sediment transport bidimensional numerical model using PIV and 3D Scanning technologies. *Journal of Hydraulic Research* 2008; **46**(4):489–503. DOI: 10.3826/jhr.2008.2737.
3. Navarrina F, Colominas I, Casteleiro M, Cueto-Felgueroso L, Gómez H, Fe J, Soage A. A numerical model for the transport of salinity in estuaries. *International Journal for Numerical Methods in Fluids* 2008; **56**:507–523.
4. Bonillo J, Puertas J, Fe J, Vellando P. A 2D numerical model for the transport of pollutants. The influence of boundary conditions. *3rd International Symposium on Ecohydraulics*, Salt Lake City, UT, 1999.
5. Alcrudo F. A state of the art review on mathematical modelling of flood propagation. *Report of the Investigation of Extreme Flood Processes and Uncertainty* (*IMPACT*). Available on the web at: www.samui.co.uk/impact-project/.
6. Cea L, French JR, Vázquez-Cendón ME. Numerical modelling of tidal flows in complex estuaries including turbulence: an unstructured finite volume solver and experimental validation. *International Journal for Numerical Methods in Engineering* 2006; **67**:1909–1932.
7. Bermúdez A, Dervieux A, Desideri J, Vázquez ME. Upwind schemes for the two dimensional shallow water equations with variable depth using unstructured meshes. *Computer Methods in Applied Mechanics and Engineering* 1998; **155**:49–72.
8. Vázquez-Cendón ME. Improved treatment of source terms in upwind schemes for the shallow water equations in channels with irregular geometry. *Journal of Computational Physics* 1999; **148**:497–526.
9. Alcrudo F, García-Navarro P. A high resolution Godunov type scheme in finite volumes for the 2D shallow-water equations. *International Journal for Numerical Methods in Fluids* 1993; **16**:489–505.

10. Mingham CG, Causon DM. High-resolution finite-volume method for shallow water flows. *Journal of Hydraulic Engineering* 1998; **124**(6):604–614.
11. Chippada S, Dawson CN, Martínez ML, Wheeler MF. A Godunov-type finite volume method for the system of shallow water equations. *Computer Methods in Applied Mechanics and Engineering* 1998; **151**:105–129.
12. Brufau P, García-Navarro P. Two-dimensional dam break flow simulation. *International Journal for Numerical Methods in Fluids* 2000; **33**:35–57.
13. Fe J, Cueto-Felgueroso L, Navarrina F, Puertas J. Numerical viscosity reduction in the resolution of the shallow water equations with turbulent term. *International Journal for Numerical Methods in Fluids*. DOI: 10.1002/fld.1759.
14. Anastasiou A, Chan CT. Solution of the shallow water equations using the finite volume method on unstructured triangular meshes. *International Journal for Numerical Methods in Fluids* 1997; **24**:1225–1245.
15. Rastogi A, Rodi W. Predictions of heat and mass transfer in open channels. *Journal of the Hydraulics Division. Proceedings of the American Society of Civil Engineers* 1978; **104**(HY3):397–418.
16. Launder BE, Spalding DB. The numerical computation of turbulent flows. *Computer Methods in Applied Mechanics and Engineering* 1974; **3**:269–289.
17. McGuirk JJ, Rodi W. A depth-averaged mathematical model for the near field of side discharges into open-channel flow. *Journal of Fluid Mechanics* 1978; **86**(part 4):761–781.
18. Rodi W, Pavlovic N, Srivatsa SK. Prediction of flow and pollutant spreading in rivers. *Transport Models for Inland and Coastal Waters*. Academic Press: New York, 1981; 63–111.
19. Falconer RA, Guiyi L. Modelling tidal flows in an island's wake using a two-equation turbulence model. *Proceedings of the Institution of Civil Engineers. Water, Maritime and Energy* 1992; **96**(1):43–53. DOI: 10.1680/iwtme.1992.18497.
20. Rameshwaran P, Shiono K. Predictions of velocity and boundary shear stress in compound meandering channel. *River Flow* 2002; **1**:223–231.
21. Minh B, Wenka T, Rodi W. Numerical modelling of bed deformation in laboratory channels. *Journal of Hydraulic Engineering* 2004; **130**(9):894–904.
22. Chaudhry MH. *Open Channel Flow*. Prentice-Hall: Englewood Cliffs, NJ, 1993.
23. Harten A, Lax P, Van Leer B. On upstream differencing and Godunov-type schemes for hyperbolic conservation laws. *SIAM Review* 1983; **25**:35–61.
24. Brufau P, Vázquez-Cendón ME, García-Navarro P. A numerical model for the flooding and drying of irregular domains. *International Journal for Numerical Methods in Fluids* 2002; **39**:247–275.
25. Burguete J, García-Navarro P, Murillo J. Friction term discretization and limitation to preserve stability and conservation in the 1D shallow-water model: application to unsteady irrigation and river flow. *International Journal for Numerical Methods in Fluids* 2007; DOI: 10.1002/fld.1727.
26. Rodi W. *Turbulence Models and their Application in Hydraulics. A State-of-the-art Review*, *IAHR Monograph* (3rd edn). Balkema: Rotterdam, 1993.
27. Nezu I, Nakagawa H. *Turbulence in Open-channel Flows. IAHR Monograph*. Balkema: Rotterdam, 1993.
28. Fischer H, List E, Koh R, Imberger J, Brooks N. *Mixing in Inland and Coastal Waters*. Academic Press: New York, 1979; 105–112.
29. Fe J. Aplicación del método de volúmenes finitos a la resolución numérica de las ecuaciones de aguas someras con incorporación de los esfuerzos debidos a la turbulencia. *Ph.D. Dissertation* (in Spanish), University of A Coruña, 2005. Available on the web at: http://www.tesisenred.net/.
30. Finnie JI, Jeppson RW. Solving turbulent flows using finite elements. *Journal of Hydraulic Engineering* 1991; **117**(11):1513–1530.
31. Wilcox D. *Turbulence Modelling for CFD*. DCW Industries, Inc.: La Cañada, CA, 2002.
32. Versteeg H, Malalasekera W. *An Introduction to Computational Fluid Dynamics. The Finite Volume Method*. Addison-Wesley Longman: Harlow, 1995.
33. Spalding DB. A single formula for the law of the wall, Transactions of the ASME Series A. *Journal of Applied Mechanics* 1961; **28**(3):444–458.
34. Tucker PG. Prediction of turbulent oscillatory flows in complex systems. *International Journal for Numerical Methods in Fluids* 2000; **33**:869–895.
35. Goncalves E, Houdeville R. Turbulence model and numerical scheme assessment for buffet computations. *International Journal for Numerical Methods in Fluids* 2004; **46**:1127–1152.
36. Brigham Young University. *User's guide to RMA2 version 4.3*, Salt Lake City, U.S.A., 1996.
37. Leschziner M, Rodi W. Calculations of strongly curved open channel flow. *Journal of the Hydraulics Division. Proceedings of the American Society of Civil Engineers* 1979; **105**(HY10):1297–1314.

38. Codina R, Soto O. Finite element implementation of two-equation and algebraic stress turbulence models for steady incompressible flows. *International Journal for Numerical Methods in Fluids* 1999; **30**:309–333.
39. Ferziger J, Peric M. *Computational Methods for Fluid Dynamics*. Springer: Berlin, 1996.
40. Ruiz D. Ensayos experimentales y simulación numérica de problemas de dinámica de fluidos. *Technical Report*, University of La Coruña, 2006 (in Spanish).
41. Chow VT. *Open-channel Hydraulics*. McGraw-Hill: New York, 1959.
42. Thangam S. Analysis of two equation turbulence models for recirculating flows. *NASA Contractor Report 187607, ICASE Report No. 91-61*, 1991.

DOI: 10.1002/fld